

# Analyzer-less X-ray Interferometry with Super-Resolution Methods

Murtuza S. Taqi<sup>1</sup>, Hunter C. Meyer<sup>1</sup>, and Joyoni Dey<sup>1\*</sup>

<sup>1</sup>Department of Physics and Astronomy, Louisiana State University, Baton Rouge, LA, 70803

\*Corresponding Author: deyj@lsu.edu

## Abstract

X-ray interferometry provides valuable information in terms of attenuation, small-angle scatter, and differential phase contrast. This multi-modal contrast can aid in many clinical applications, such as lung diseases and breast cancer. However, standard interferometry has an analyzer grating that can increase the dose requirement to maintain the same image quality as a standard X-ray. We propose the use of super-resolution methods for X-ray grating interferometry without an analyzer, with detectors that fail to meet the Nyquist sampling rate needed for traditional image recovery algorithms. We use the phase-steps judiciously to nominally recover the sampling and iteratively recover the visibility and the object parameters. This method enables Talbot-Lau interferometry without the X-ray absorbing analyzer. It also allows for smaller fringe periods ( $P_d$ ) or higher autocorrelation lengths for the analyzer-less Modulated Phase Grating Interferometer. This will allow for reduced X-ray dose and higher autocorrelation lengths than previously accessible. We demonstrate the use of super-resolution methods to iteratively reconstruct attenuation, differential-phase, and dark-field images using simulations of two-dimensional lung phantoms with lesions. We tested a direct detector with 75  $\mu\text{m}$  and 30  $\mu\text{m}$  pixel size, modeled using a box-binning. We also tested scintillator-based detectors with 50  $\mu\text{m}$  and 75  $\mu\text{m}$  pixel sizes, modeled using Gaussian PSFs. We show that our super-resolution iterative reconstruction methods are robust to noise and can be used to improve grating interferometry for cases where traditional algorithms cannot be used.

## 1. Introduction

X-ray grating interferometry is a phase-sensitive imaging technique that simultaneously captures attenuation, differential-phase, and dark-field images. The attenuation image shows X-ray absorption, similar to a traditional radiograph, while the differential-phase and dark-field images are related to X-ray refraction and small angle scatter. With the introduction of differential-phase and dark-field images, X-ray interferometry has a wide variety of potential applications, including lung imaging [1–4], breast imaging [5–8], arthritis imaging [9, 10], osteoporosis imaging [11], additive manufacturing quality assurance [12, 13] and porosimetry [14].

Various types of interferometers exist, Dual-phase Grating Interferometer(DPGI), Modulated Phase Grating Interferometer(MPGI), and the most prevalent for biomedical imaging applications, the Talbot-Lau Interferometer (TLI). The TLI is at the forefront of preclinical and clinical studies for lung and breast imaging [1–10]. The traditional Talbot-Lau Interferometer (TLI) [15–18], as shown in Figure 1a, uses a binary phase grating (labeled G1) to produce a high-resolution fringe pattern that cannot be resolved by traditional X-ray detectors. A second grating (labeled G2) serves as an analyzer grating to resolve the sub-pixel fringe patterns. However, since the analyzer is an absorption grating, about half of the X-rays are absorbed. Depending on parameters, this may require a dose increase as much as factor of 5 [19].

The Modulated Phase Grating Interferometer (MPGI), as shown in Figure 1b, uses a single modulated phase grating to produce directly resolvable fringe patterns [20–24] without the need for an analyzer grating. Since the MPGI does not require an analyzer grating, the interference fringes have to be resolved directly at the detector. This means that the fringe period at the detector,  $P_d$ , must be at least twice the detector pixel size to meet the Nyquist criterion. The MPG has bar heights that follow an envelope function with a period,  $W$ . The envelope function is sampled at a high frequency pitch,  $p$ , to

maintain the same coherence requirements as that of the TLI. The autocorrelation length is given by  $ACL = \lambda D_{OD}/P_d$ , where  $\lambda$  is the peak wavelength,  $D_{OD}$  is the object-to-detector distance, and  $P_d$  is the fringe period. MPGI systems with larger  $W$  will have a larger  $P_d$  which leads to a smaller ACL. The ACL is important for dark-field imaging of porous objects, since the ACL determines the amount of dark-field signal produced by different scattering structures [24–26]. To increase the ACL, therefore, a small- $W$  MPGI and hence smaller  $P_d$  is necessary, which will ideally require a smaller detector pixel size to resolve.

In this paper, we employ super-resolution methods [27] that can benefit grating based interferometry, for both the TLI and MPGI, which we explain in a later paragraph. The term super-resolution refers to the process of sub-pixel sampling, achieved by incrementally stepping the detector and subsequently applying iterative reconstruction methods to recover the image parameters. This work generally reflects the strategy presented in Gutman et al.[28] and other super-resolution applications which combines multiple low-resolution (LR) images to reconstruct a high-resolution (HR) image. However, our approach necessarily differs from that of Gutman et al work in that a central component is our *imaging* framework, which is pixel localization of attenuation, dark-field and differential phase. Super-resolution methods have been used by scientists/engineers for decades for various applications [27–29], including angular super-resolution with standard X-ray systems to measure small-angle X-ray scattering (SAXS) data [28]. Notably, the work in Gutman et al [28] provides the angular distribution of SAX, without the spatial localization information afforded by grating-based interferometric dark-field imaging, the focus of our present work.

In standard interferometry, where  $P_d$  is adequately sampled through the analyzer, one of the gratings is typically stepped without the object (reference) and then with the object [17, 30]. Two phase-stepping curves are obtained at each pixel, one with and without the object. From the two curves, the attenuation, dark-field (related to small-angle X-ray scatter), and the differential phase of the object are estimated [31].

In our method, the phase-stepped images, obtained by stepping the detector, comprise the low-resolution (LR) images, which are then interlaced. Explicit forward model and iterative reconstruction are employed to recover the attenuation, differential-phase, and dark-field images for lung imaging applications. We propose that, if the required fringe pattern is undersampled by the detector, the phase stepped images are instead interlaced to nominally recover the sampling for the reference and with-object signals. Then the visibility loss is retrieved for the reference signal, which in turn is used to compare with the with-object signal to estimate the object attenuation, darkfield, and differential-phase.

For TLI, super-resolution enables imaging with the analyzer grating, thereby reducing X-ray dose. Without the analyzer, the fringe period at the detector,  $P_d$ , must be resolved depends on the pitch of the G1 grating and its magnification under the cone-beam geometry. The super-resolution method allows this  $P_d$  to be smaller than the detector pixel size. Consequently, the analyzer-less method becomes feasible for many cases where fringes would otherwise not be directly resolvable. In this work, we calculate several potential analyzer-less TLI geometries for lung imaging, where  $P_d$  and object parameters can be recovered through the super-resolution method. Eliminating the analyzer grating also reduces system cost and simplifies experimental alignment.

The MPGI system is analyzer-less by design. For MPGI, the fringe period at the detector,  $P_d$ , corresponds to the projected envelope period,  $W$ , of the modulated phase grating. The super-resolution method allows a fringe period  $P_d$  smaller than the detector pixel size, enabling lower  $P_d$  and thus higher autocorrelation length (ACL) suitable for lung imaging. Such high ACL imaging can be achieved by small- $W$  MPGI. We provide example geometries demonstrating these configurations.

Our method is novel in that it applies super-resolution techniques to grating interferometry to resolve fringes without an analyzer. To the best of our knowledge no one has attempted this before. Improvement of resolution also comes automatically with the method. The effective resolution can be as high as the phase-step resolution (sub-detector pixel) instead of the pixel size.

In addition to reducing the X-ray dose for the TLI and enabling higher ACL for the MPGI, iterative reconstruction involved in our super-resolution can improve resolution and reduce noise in the reconstructed projection images.

The key focus of this work is to apply iterative reconstruction to initially recover the *projection images* for the three modalities, particularly when acquired under undersampled conditions. For cases with multiple projection angles in tomographic interferometry, additional processing with standard 3D

analytical or established iterative 3D reconstruction techniques can be applied.

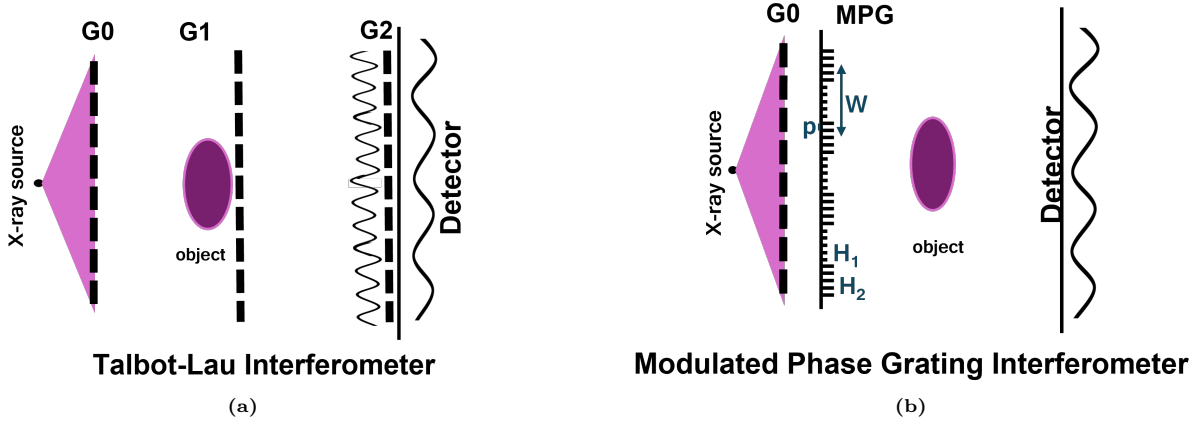


**Figure 1.** Schematics of the (a) Talbot-Lau Interferometer Schematic, with three gratings G0,G1 and G2 (analyzer) and (b) Modulated Phase Grating Interferometer Schematic with no G2 grating. The G1 grating has modulation of width  $W$  and pitch  $P$ .

## 2. Methods

The work involves (1) simulation of a lung interferometry phantom and an under-sampled interferometry acquisition scenario, and (2) a recovery method.

### 2.1. Synthetic Phantom and Interferometry Image Generation

Two-dimensional interferometry signals are simulated at sub-pixel phase steps by calculating the interference fringes with and without the object in place, referred to as the ‘reference’ and ‘object’ signals. The simulations are system agnostic (that is, they apply to Talbot-Lau Interferometry or Modulated Phase Grating), and the signals are approximated as perfect sinusoids. The source and detector blur are then applied, detector sub-sampling is simulated, and Poisson noise is added. The reference image for each phase step is calculated using Eqn. 1, where  $A(x, y)$  is the per-pixel amplitude of the fringe pattern,  $B(x, y)$  is the per-pixel bias,  $t_k(x, y)$  is the per-pixel translation of the  $k$ -th phase step, and  $P_d$  is the fringe period at the detector. The fringe visibility is represented as  $A(x, y)/B(x, y)$ .

$$g_r^k(x, y) = A(x, y) \cos \left[ \frac{2\pi}{P_d} (x + t_k) \right] + B(x, y) \quad (1)$$

Note that reference  $g_r^k(x, y)$  is a 2D image but the grating is only in one direction. The object image is simulated similarly, as shown in Eqn. 2, where  $e^{-\mu T(x, y)}$  represents the object attenuation,  $t_{ph}(x, y)$  represents the phase shift due to refraction, and  $e^{-S(x, y)}$  represents the visibility loss due to small angle scatter. The phase shift due to refraction,  $t_{ph}(x, y)$ , is represented as  $t_{ph}(x, y) = \frac{\lambda}{2\pi} \frac{\partial \varphi(x, y)}{\partial x} D_{OD}$  where  $D_{OD}$  is the object-to-detector distance and  $\frac{\partial \varphi(x, y)}{\partial x}$  is the partial derivative of the phase. Unlike traditional interferometry, we phase step the *detector*, not the grating, to achieve sub-pixel resolution. Hence, each term is also shifted by  $t_k$ , since it is the detector that is shifted for phase stepping, not the grating.

$$g_{obj}^k(x, y) = \left\{ A(x, y) e^{-S(x+t_k, y)} \cos \left[ \frac{2\pi}{P_d} (x + t_{ph}(x) + t_k) \right] + B(x, y) \right\} e^{-\mu T(x+t_k, y)} \quad (2)$$

To simulate phase-stepping of the detector, the generated signals  $g_r^k(x, y)$  and  $g_{obj}^k(x, y)$  are shifted by the step resolution  $t_k$  which typically is in the order of a few microns.

The  $A(x, y)$ ,  $B(x, y)$  are chosen as constants when generating the simulated images. In the iterative model-fitting recovery algorithm described later, they are assumed to be varying pixel-wise.

Two different detectors were tested. For a direct detector, box-binning was used to simulate detector blur. For indirect detectors (for example, scintillator), blurring by a Gaussian PSF is more appropriate.

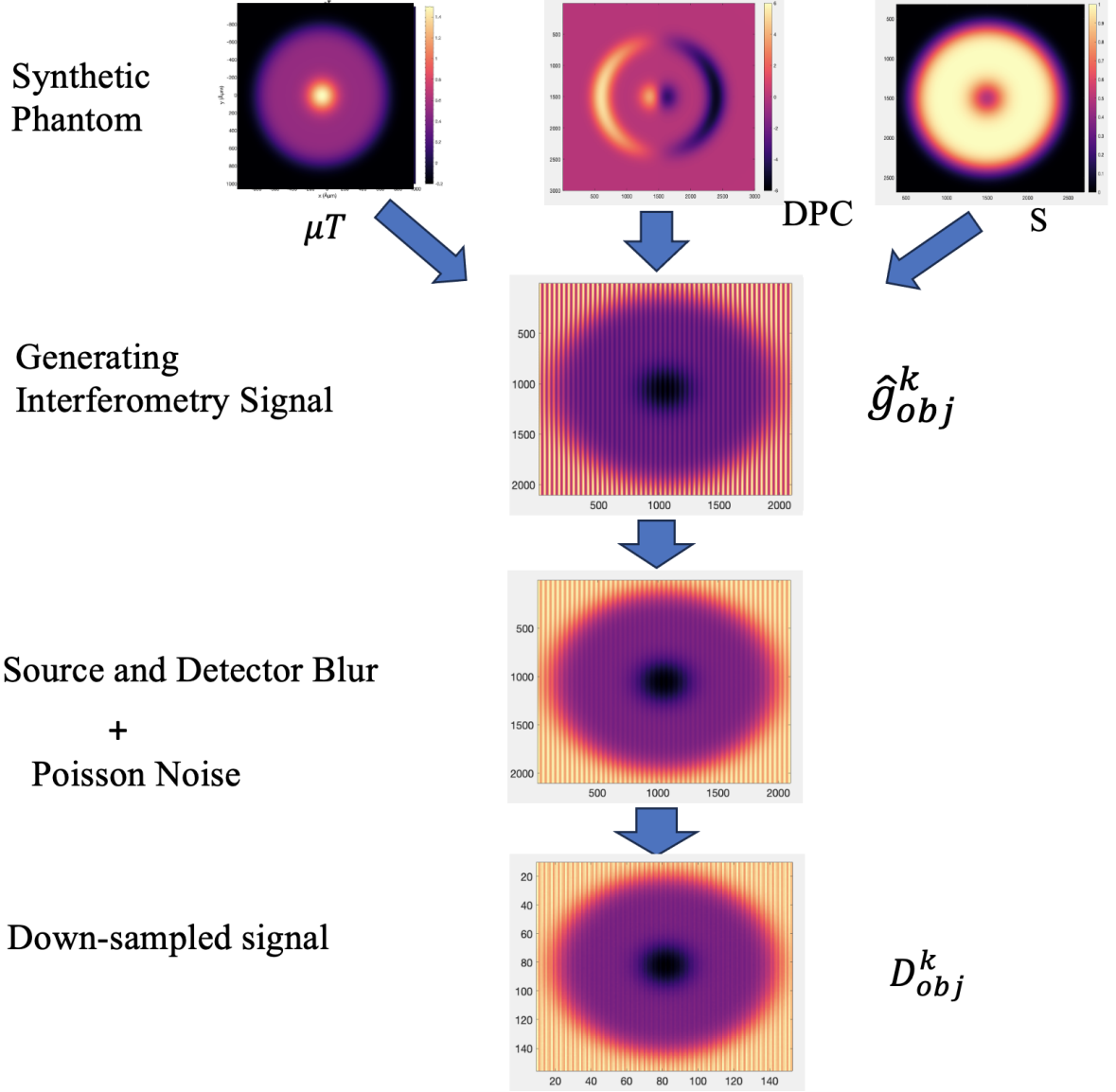


**Figure 2.** Flowchart of the Phantom generation with known ground truth of  $\mu T$ , dark field parameter,  $S$  and differential phase-shift(DPC). The interferometry signal is generated by using equation 2 by using the above defined parameters. The phase step is obtained by translation of interferometry pattern, but for illusion purposes, only a single phase-step is shown.

For the direct detector case, along with source blur, detector blur was applied with detector binning approach to simulate sharp pixel boundaries, and is shown in Eqns. 3 and 4.

$$D_r^k(x, y) = [g_r^k(x, y) \star \star s(x, y)]_{DetectorBinning} + noise(x, y) \quad (3)$$

$$D_{obj}^k(x, y) = [g_{obj}^k(x, y) \star \star s(x, y)]_{DetectorBinning} + noise(x, y) \quad (4)$$

Poisson noise is added to the  $k$ -th phase step signal after detector binning to the detector pixel rate to get  $D_r^k(x, y)$  and  $D_{obj}^k(x, y)$ . These simulate the acquired (under-sampled) phase-steps.

For the indirect detector case, the source blur and detector blur are applied by two-dimensional convolution of the “pure” signals with the source profile,  $s(x, y)$ , and detector point spread function,  $PSF(x, y)$ , as shown in Eqns. 5 and 6, where  $\star \star$  represents the two-dimensional convolution.

$$D_r^k(x, y) = [g_r^k(x, y) \star \star s(x, y) \star \star PSF(x, y) + noise(x, y)]_{\downarrow} \quad (5)$$

$$D_{obj}^k(x, y) = [g_{obj}^k(x, y) \star \star s(x, y) \star \star PSF(x, y) + noise(x, y)]_{\downarrow} \quad (6)$$

Poisson noise is added to the  $N$  phase step signals and down-sampled (indicated by the  $\downarrow$ ) to the

detector pixel rate to get  $D_r^k(x, y)$  and  $D_{obj}^k(x, y)$ . They are then used as inputs into the image recovery algorithm for the iterative reconstruction of  $\mu T(x, y)$ ,  $S(x, y)$ , and  $t_{ph}(x, y)$ .

Specific parameters are detailed in section 2.3.

## 2.2. Image Recovery

The image recovery algorithm is broken into two stages- *interlacing the phase steps* and *reconstruction* as shown in Figures 3 and 4. This combined technique is referred to as super-resolution that lead us to perform analyzer-less X-ray interferometry.

### 2.2.1. Interlacing

The acquired detector signals or phase steps  $D_{obj}^k(x, y)$  (each of size, say  $n \times m$ ) are interlaced in the x-direction to obtain object image with nominal sub-pixel sampling of size  $n \times Nm$ . This process is shown in Figure 3. Specifically, the first columns from phase steps  $k=1$  to  $N$  are sequentially appended, followed by the second columns from each phase step, and so on, until all the columns have been assembled. This results in a larger  $n \times Nm$  image,  $I_{obj}(x, y)$ . The same procedure is applied to the reference phase steps  $D_r^k(x, y)$ , producing a similarly interlaced  $I_r(x, y)$ .

At this stage, the interlaced images,  $I_r(x, y)$  and  $I_{obj}(x, y)$  are nominally sampled in the x-direction at the phase stepping resolution. The term nominal is used because even though the resolution is now higher and aliasing is nominally mitigated, the pixel blur remains, substantially reducing fringe visibility. This makes it difficult or impossible to recover the differential-phase and dark-field images using conventional algorithms at this stage. To address this, we apply an iterative reconstruction algorithm to recover the visibility from the reference image  $I_r(x, y)$ , and use the visibility-restored reference in turn iteratively to recover the attenuation, differential-phase, and dark-field images from  $I_{obj}(x, y)$ , as detailed next.

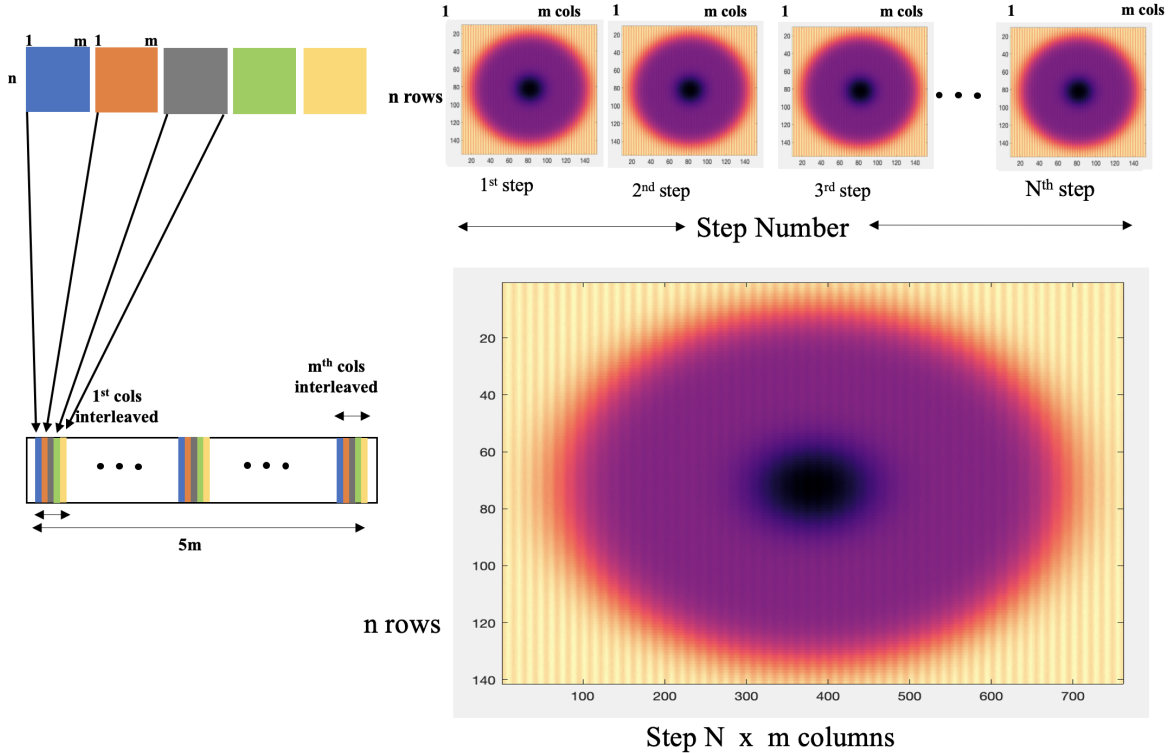


**Figure 3.** Left: Schematic representation of interlacing five phase-stepped images,  $D_{obj}^k(x, y)$ ,  $k = 1 \dots 5$ , each with dimension  $n \times m$ . The first columns from all five images are concatenated in order, followed by the second columns, and so on, until the last or  $m$ -th column. The resulting image,  $I_{obj}(x, y)$ , has dimensions  $n \times 5m$ . Note: Although the phase-stepped images are shown in distinct colors for illustrative purposes, they are nearly identical in intensity in practice (representing either a set of reference phase steps or reference+object phase steps). The observed intensity variations arise primarily from sub-pixel phase shifts on the order of a few microns. Right: Figure shows the same process for the down-sampled interferometry signal. The downsampled signal,  $D_{obj}^k(x, y)$ , is interlaced to generate the interlaced image,  $I_{obj}(x, y)$

### 2.2.2. Iterative Reconstruction

Reconstruction of the images was performed in two stages as shown in Figure 4.

The first stage is the removal of the detector blur from the noisy reference image,  $I_r(x, y)$ , illustrated in Figure 4a. Direct deconvolution produced oscillations and/or introduced apodization errors, so we performed this step iteratively, as is commonly done in super-resolution literature [27]. The goal is to recover a visibility-restored estimate of the reference image,  $\hat{g}_r(x, y)$ , that has no detector blur. This was done by iteratively fitting the initial parameters,  $[\hat{A}(x, y), \hat{B}(x, y), \hat{\phi}_0(x, y)]$ , where  $\hat{\phi}_0$  is the phase of the initial reference pattern. While  $\phi_0(x, y)$  is not needed in the image simulation, real experimental data would have an arbitrary phase, so  $\hat{\phi}_0(x, y)$  must be included. Starting with an initial estimate,  $\hat{g}_r(x, y)$  is calculated and detector blur is applied. The sum squared error (SSE) is calculated and minimized by iteratively updating  $[\hat{A}(x, y), \hat{B}(x, y), \hat{\phi}_0(x, y)]$  using *fmincon* in Matlab until convergence is achieved.

The second stage, illustrated in Figure 4b, is the recovery of  $\mu T(x, y)$ ,  $t_{ph}(x, y)$ , and  $S(x, y)$  by iterative reconstruction, using the visibility-restored reference from Stage 1 in the forward model.

Starting with an initial estimate of  $\mu T(x, y)$ ,  $S(x, y)$  and  $t_{ph}(x, y)$ , the forward model  $\hat{g}_{obj}(x, y)$  is used to calculate the expected fringe pattern (that contains no pixel blur), shown in Eqn. 7. Note the parameters  $[\hat{A}, \hat{B}, \hat{\phi}_0]$  finalized visibility-restored reference parameter from Stage 1, and the object parameters are used to construct the  $\hat{g}_{obj}(x, y)$ . To be able to compare with the real image,  $I_{obj}(x, y)$ , the blur is then simulated by convolution, producing the expected measurement,  $\hat{I}_{obj}(x, y)$ . The  $\hat{I}_{obj}(x, y)$  and  $I_{obj}(x, y)$  are then compared using a given metric and the metric optimized.

The form of Eqn. 2 suggests that  $\mu T(x, y)$  can be estimated first, followed by  $t_{ph}(x, y)$  and  $S(x, y)$ . This is like the standard method of estimation, Marathe et al [31] where the three parameters are estimated in order, with the attenuation estimated from zeroth-frequency information first and the small angle scatter is estimated from first harmonic after normalizing from attenuation effects. Moreover, because  $\mu T(x, y)$  attenuates both the bias and the amplitude, (and it can be estimated from the average or the bias), it is the least noisy component, whereas  $S(x, y)$  affects only the amplitude and is therefore more prone to noise.

The model parameters were estimated using multiple optimization strategies (adaptive gradient descent, newton's method, quasi-newton method), and two metrics - the Maximum likelihood function (ML) and the Huber loss, with particular emphasis on balancing computational efficiency and accuracy. Among the tested approaches, those that achieved the fastest convergence while maintaining high fidelity were selected. This led to the different methods being optimal for the three modalities, which is not unexpected due to the different noise-levels in the different modalities.

In Appendix A we have included the overall Root Mean Squared Errors (RMSE) and time to converge, for some of our other investigations (slower or less accurate) with different optimizers and metrics.

Specifically, the parameter  $\mu T$  was estimated using the maximum-likelihood (ML) framework, as defined in Eqn. 9, in combination with Newton's method utilizing second-order derivatives Eqn. 11. Although  $\mu T$  can alternatively be recovered using gradient descent Eqn. 12, but the latter exhibited significantly slower convergence compared to Newton's method. Consequently, Newton's method was adopted as the primary optimization approach.

The  $\mu T(x, y)$  was estimated first using the Newton method (with second derivatives) to maximize ML. Second,  $t_{ph}(x, y)$  was recovered using the adaptive gradient descent of Huber loss and lastly  $S(x, y)$  was recovered by quasi-newton minimization of Huber loss. This was implemented using *fminunc* in Matlab. In all cases needed, the derivatives and second derivatives were analytically calculated and provided explicitly.

$$\hat{g}_{obj}(x, y) = \left\{ \hat{A}(x, y) e^{-S(x, y)} \cos \left( \frac{2\pi}{P_d} \left( x + t_{ph}(x) + \hat{\phi}_0 \right) \right) + \hat{B}(x, y) \right\} e^{-\mu T(x, y)} \quad (7)$$

$$\hat{I}_{obj}(x, y) = \hat{g}_{obj}(x, y) \star \star PSF(x, y) \star \star s(x, y) \quad (8)$$

$$L(x) = I_{obj}(x) * \log \left( \hat{I}_{obj}(x) \right) - \hat{I}_{obj}(x) \quad (9)$$

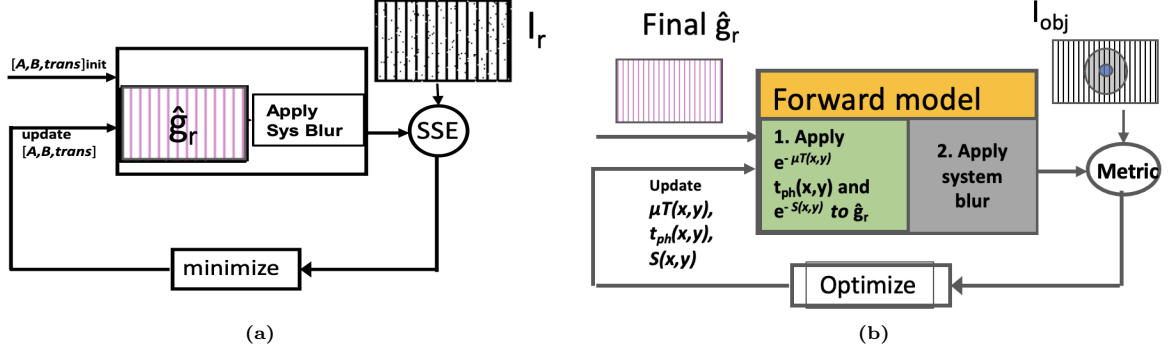


**Figure 4.** Stages 1 and 2 (a) Stage 1 to recover  $\hat{g}_r$ . This essentially recovers the visibility for the reference signal,  $I_r(x)$ . (b) Stage 2 to recover  $\mu T(x)$ ,  $t_{ph}(x)$ , and  $S(x)$ .

$$L_\delta(r) = \begin{cases} \frac{1}{2}r^2 & \text{if } |r| \leq \delta, \\ \delta (|r| - \frac{1}{2}\delta) & \text{if } |r| > \delta \end{cases}, \quad r = \hat{I}_{obj}(x) - I_{obj}(x). \quad (10)$$

$$\mu T_{i+1} = \mu T_i + \frac{\nabla_{\mu T} L(\mu T_i)}{\nabla_{\mu T}^2 L(\mu T_i)} \quad (11)$$

For the recovery of  $t_{ph}(x)$ , the best recovery was performed by using Huber Loss as defined in Eqn. 10 using the gradient descent method. ML also performs well but takes longer to converge and requires a stronger tuning of the learning rate,  $\lambda$ , for individual cases. Newton's method and Quasi-Newton BFGS method were also tested but gradient descent performs the best.

$$t_{ph, i+1}(x) = t_{ph, i}(x) + \lambda_i \frac{\partial L(x)}{\partial t_{ph, i}(x)} \quad (12)$$

$$(13)$$

where  $\lambda_i$  represents the learning rate.

For the recovery of  $S$ , the fastest and most accurate result was obtained using Huber Loss and using Quasi Newton method as defined in Eqn. 14.

$$S_{i+1} = S_i - \alpha_i B_i^{-1} \nabla_S L(S_i; x) \quad (14)$$

here the objective function (Huber loss in this case) is denoted by  $L(S; x)$ , and  $\nabla_S L(S_i; x)$  is the gradient of  $L$  with respect to  $S$  evaluated at iteration  $i$ . The matrix  $B_i$  is an approximation to the Hessian  $\nabla_S^2 L(S_i; x)$ , and  $\alpha_i$  is the step size, often determined using a line search.

In this work, the quasi-Newton updates were performed for  $S$  using MATLAB's `fminunc` function, which employs a BFGS-type [32] update for efficiency.

Since the derivative involves the oscillatory intensity, it is smoothed via convolution by a window of width  $2P_d$  to  $4P_d$  so that the parameter estimates do not oscillate in  $x$ .

### 2.3. Simulation Parameters

*Phantom Simulation:* The object simulated is a virtual lung phantom of size 10mm x 10mm with a thickness of  $T = 10$  cm, with "lesion", "non-lesion" or "lung" and air regions. These three regions can be visualized in the Figure 5(a) as three distinct regions. For the non-lesion region or "lung" region, an attenuation coefficient of  $\mu = 0.06675$  cm<sup>-1</sup> was used, from the NIST XCOM database of lungs at 40 keV [33]. In this region,  $S = 1$  was used to represent healthy lungs, found using the normalized dark-field coefficient of  $R = 1.5$  from [25]. The real part of the index of refraction was  $\delta = 1.82 \times 10^{-7}$ , found by scaling the value from [34] from 33 keV to 40 keV. The "lesion" was added with a maximum thickness of 5 cm. At their peak, the lesion has an attenuation coefficient of  $\mu = 0.25$  cm<sup>-1</sup>, produces no visibility

loss due to SAXS, and  $\delta = 4 * 10^{-7}$ . These values were chosen to best represent the effects of lesion soft tissue (higher density and no small-angle scatter). The lesion is incorporated into the virtual phantom by partially replacing the lung tissue and leaving behind the rest of the lung. For example, the peak  $\mu T$  ( $\mu \times$  thickness for the 5 cm tumor was 1.58. This comes from 5 cm of lesion and 5 cm of non-lesion tissue.

**Table 1.** TLI and MPGI setups that produce the following  $P_d$  and  $ACL = 0.564 \mu m$ . The visibility is *before* detector blur for a 40 keV.

System	$P_d$ ( $\mu m$ )	Source-to-Grating Distance	Grating-to-Detector Distance	Visibility
TLI	22	71 mm	710 mm	69.4%
MPGI	22	887 mm	1065 mm	53.6%
MPGI	55	197 mm	887 mm	50%

*Image Generation:* In this work, the simulations performed are system agnostic since the only required parameters for Eqn. 7 are the desired bias, visibility, fringe period, and step resolution. In this work, we use detector size of  $75 \mu m$  and  $50 \mu m$ . We also show one case of detector size of  $30 \mu m$  as a demonstration for using a lower  $P_d$ .

Even if system agnostic, possible system geometries are shown for TLI and MPGI in Table 1 for 40 keV (which could be the peak for a 70kVp setting). For TLI systems without an analyzer,  $P_d$  is a magnified version of the fringe patterns created by  $p_1$ , the period of G1, which are only few microns. For MPGI similarly,  $P_d$  is related to the magnified version of envelope modulation  $W$ . In Table 1, the visibility is calculated from Fresnel approximate fast SRDI simulations of fringes [23, 24].

For 60 keV operation, other TLI geometries yielded detector fringe periods of  $P_d = 13 \mu m$  and  $P_d = 22 \mu m$ . A configuration producing  $P_d = 13 \mu m$  uses a G0–G1 distance of 22.5 cm and a G1–detector distance of 85.4 cm (Talbot order n=1) with a G1 pitch of  $5.4 \mu m$ . A geometry producing  $P_d = 22 \mu m$  uses a G0–G1 distance of 44.5 cm and a G1–detector distance of 208 cm (Talbot order n=1) with a G1 pitch of  $7.82 \mu m$ .

Even though the visibility before detector blur was high, we conservatively used a visibility of 20% in our direct detector simulations to account for some of the effects not simulated, such as the visibility loss due to Compton scatter. The phase-stepped images were simulated Eqn. 5 and Eqn. 6 for  $75 \mu m$  detector with box-binning. The simulations have an initial resolution of  $5 \mu m$ . The phase stepping was simulated at  $5 \mu m$  (number of phase-steps N=15) and  $15 \mu m$  resolution (number of phase-steps N = 5). The number of phase steps was equal to the pixel size divided by the step resolution. The simulation parameters are organized in Table 2.

*Noise:* The Poisson noise was simulated at levels determined by analyzing the signal-to-noise ratio (SNR) in previous experiments [24]. Due to calibration, the mean intensity could not be used due to a calibration scale factor. Therefore, we focused on the  $SNR = \text{mean}/\text{std} = \sqrt{N}$  to arrive at the effective bias count, N. The measured SNR was approximately 200 for each phase step image. Assuming Poisson noise, this indicates about 40K counts (pre-calibration). The images were taken under low-dose operation, with a Microfocus X-ray tube running at a  $55 \mu A$  current and 40 kVp voltage for 20-second exposures. The bias was adjusted for different phase steps to keep the total counts the same as the aforementioned case. To keep total counts over all phase steps about the same as the experimental case (N=25), the simulations were scaled by number of phase steps. For N=15, bias counts = 67K for each step was used and for N = 5, bias counts = 200K for each step.

Gaussian blur PSF was used for a  $75 \mu m$  scintillating detector. Since this is a stronger blur and washes away the fringes, the limiting  $P_d$  for each case was calculated from the literature [30]. The visibility drop is given by the following equation which models the source blur as a gaussian but it can be extended to model detector blur.

$$V = e^{(-1.887 w/p_2)^2} \quad (15)$$

where  $w$  is the FWHM of the source PSF and  $p_2 = P_d$  is the fringe period at the detector (without the analyzer for Talbot Lau case). Empirically, the smallest visibility (post-blur) that our algorithm can handle is about 2%. The initial visibility prior to blurring was set to 30% for  $75 \mu m$  detector period of  $P_d = 200 \mu m$ . The signal was subsequently blurred using a Gaussian kernel with  $\sigma = 70 \mu m$ , resulting in a visibility reduction to only approximately 2.5%. This strong blurring was selected as a worst-case scenario, representative of a detector with an effective resolution of  $75 \mu m$  and  $P_d = 200 \mu m$ .

The super-resolution approach performs progressively well with higher-resolution detectors and is therefore capable of recovering lower values of  $P_d$ . As an illustration, the case of a detector with  $50 \mu\text{m}$  resolution and  $P_d = 140 \mu\text{m}$  with a  $\sigma = 50 \mu\text{m}$  is also demonstrated.

**Table 2.** Simulation parameters.

Direct Detectors			Indirect Detectors		
Fringe Period $P_d$ ( $\mu\text{m}$ )	Detector Pixel ( $\mu\text{m}$ )	Step Res. ( $\mu\text{m}$ )	Fringe Period $P_d$ ( $\mu\text{m}$ )	Detector Pixel ( $\mu\text{m}$ )	Step Res. ( $\mu\text{m}$ )
13	30	2	140	50	5
22	75	5	200	75	5
55	75	5	200	75	15
55	75	15			

### 3. Results

First the reconstruction for the case of Gaussian blur detector  $50 \mu\text{m}$  with with a step resolution of  $5 \mu\text{m}$ , ( $N = 10$  phase steps) is shown. Using Eqn. 15 the limiting  $P_d$  was approximately  $P_d = 140 \mu\text{m}$ . The results of this case are shown in Figure 5. The parameters are compared with the ground truth in second row of figure.  $\mu T$  and  $S$  are recovered fairly well as evident in the Figures 5d and 5f. Recovery of DPC  $t_{ph}$  falls slightly short in the peak of the lung-air boundary but recovers well in the lesion region in the center as seen in Figure 5e. The Root-Mean-Squared-Error RMSE values from the ground truth are calculated at the middle row (after cropping the edge effects on both sides) are reported in the figure caption.

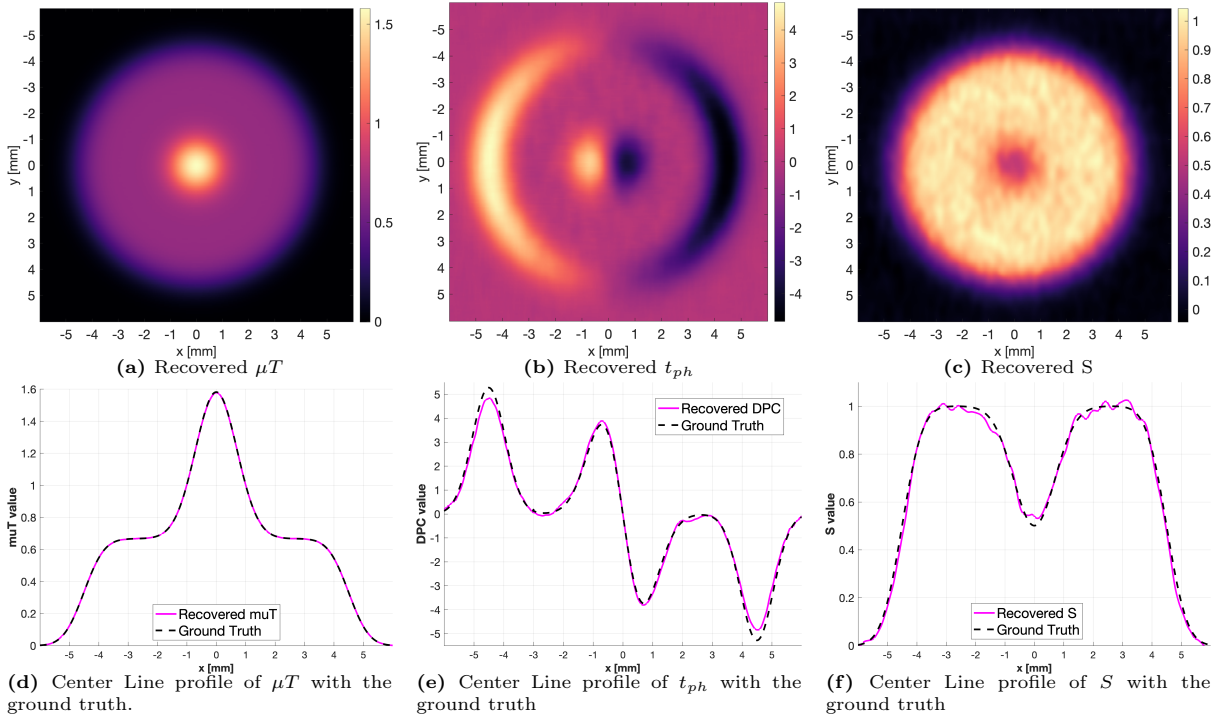


**Figure 5.** Recovered  $\mu T$ ,  $t_{ph}$ , and  $S$  for a detector of size  $50 \mu\text{m}$  and step  $N = 10$  (step-resolution =  $5 \mu\text{m}$ .  $P_d = 140 \mu\text{m}$ . The images are  $10\text{mm} \times 10\text{mm}$ . The detector model was a Gaussian PSF of  $\sigma = 50 \mu\text{m}$ . RMSE values for the middle row are  $7.7410 \times 10^{-4}$  for  $\mu T$ ,  $0.1761$  for  $t_{ph}$ , and  $0.0262$  for  $S$ .

The algorithm was tested for 4 cases for  $75 \mu\text{m}$  – two step resolutions ( $5 \mu\text{m}$ ,  $15 \mu\text{m}$ ), and two different type of detectors which are modeled by having different PSF (Box-binning and Gaussian blur). For each of these 4 cases, the three images of attenuation ( $\mu T$ ), DPC ( $t_{ph}$ ) and darkfield ( $S$ ) were recovered.

To appreciate the differences due to step-resolution or detector type, the recovered three modalities are shown separately. These results are shown in Figures 6–8. The sub-figures in these figures show the

ground truth (GT), and the recovery parameter for each of the four cases, and a line profile comparison. Each modality is considered in details next.

The Ground Truth and four reconstruction results for  $\mu T$  with a detector size of  $75 \mu m$  are presented in Figure 6. These cases comprise two simulations with a box-binning and two with a Gaussian blur, step resolution of  $15 \mu m$  and  $5 \mu m$  (using step numbers  $N = 5$  and  $N = 15$  respectively). As illustrated in the figures,  $\mu T$  is accurately recovered across all cases, a result that is further supported by the RMSE values shown in Figure 9. In all cases, the RMSE of  $\mu T$  remains within 1%.

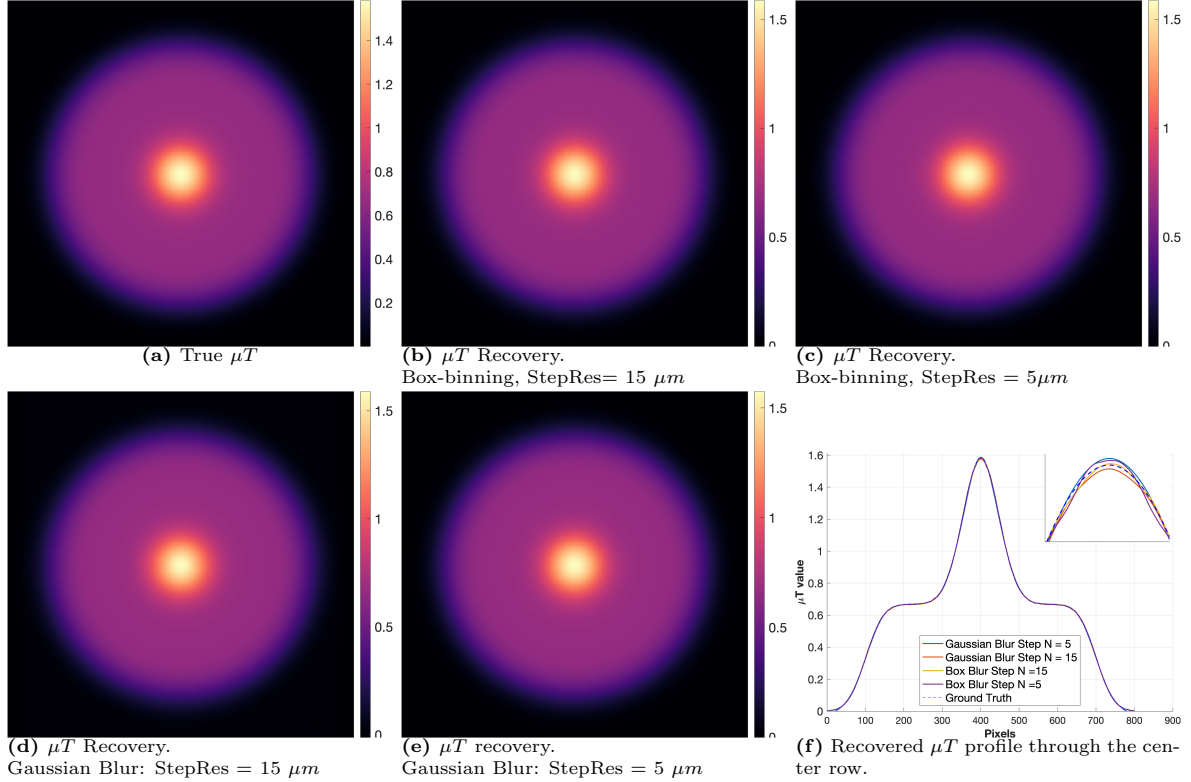


**Figure 6.** Comparison of the recovery of  $\mu T$  for four different cases compared with the Ground Truth (GT) shown in (a). The images are  $10 \text{ mm} \times 10 \text{ mm}$ . Line profiles of the center row are overlapped over each other in (f) and show the minute differences in the recovery of  $\mu T$ . The difference in the peak are highlighted in the inset included in (f)

In Figure 7, the recovery of the differential phase for the four reconstruction cases is shown. All methods recover  $t_{ph}$  accurately in the lesion region; however, the Gaussian-blur detector cases exhibit slight difficulty in reproducing the sharp peak at the lung–air boundary. This discrepancy arises from the stronger smoothing effect imposed by the Gaussian kernel. The center-line profiles compared with the ground truth, presented in Figure 7(f), illustrate this behavior. The RMSE values further confirm the trend, with the box-binning cases achieving an error of less than 6%.

The recovery of the dark-field parameter  $S$  for the four reconstruction cases is presented in Figure 8. All methods recover  $S$  reliably, with accurate performance at the lung–air boundary and within the lesion region. Some increased noise is observed in the lung parenchyma, as illustrated by the center-line profiles in Figure 8(f). The box-binning detector cases yield slightly better agreement than the Gaussian-blur cases, a trend that is further supported by the RMSE values shown in Figure 9.

The RMSE values shown in Figure 9 indicate that reconstructions with a higher number of phase steps yield lower RMSE values, even if they are originally noisier. This improvement is more pronounced in the Gaussian blur detector cases compared to the box-binning detector cases, where the fit near the edges is noisier.

The total time is less than 60 seconds and could be further optimized. The convergence times for the individual algorithms are given in the appendix.

Figure 10 shows a case of  $P_d = 13 \mu m$ , with direct detector of pixel size  $30 \mu m$ . This allows for higher ACL than  $P_d = 22 \mu m$  for same energies and object-detector distances.

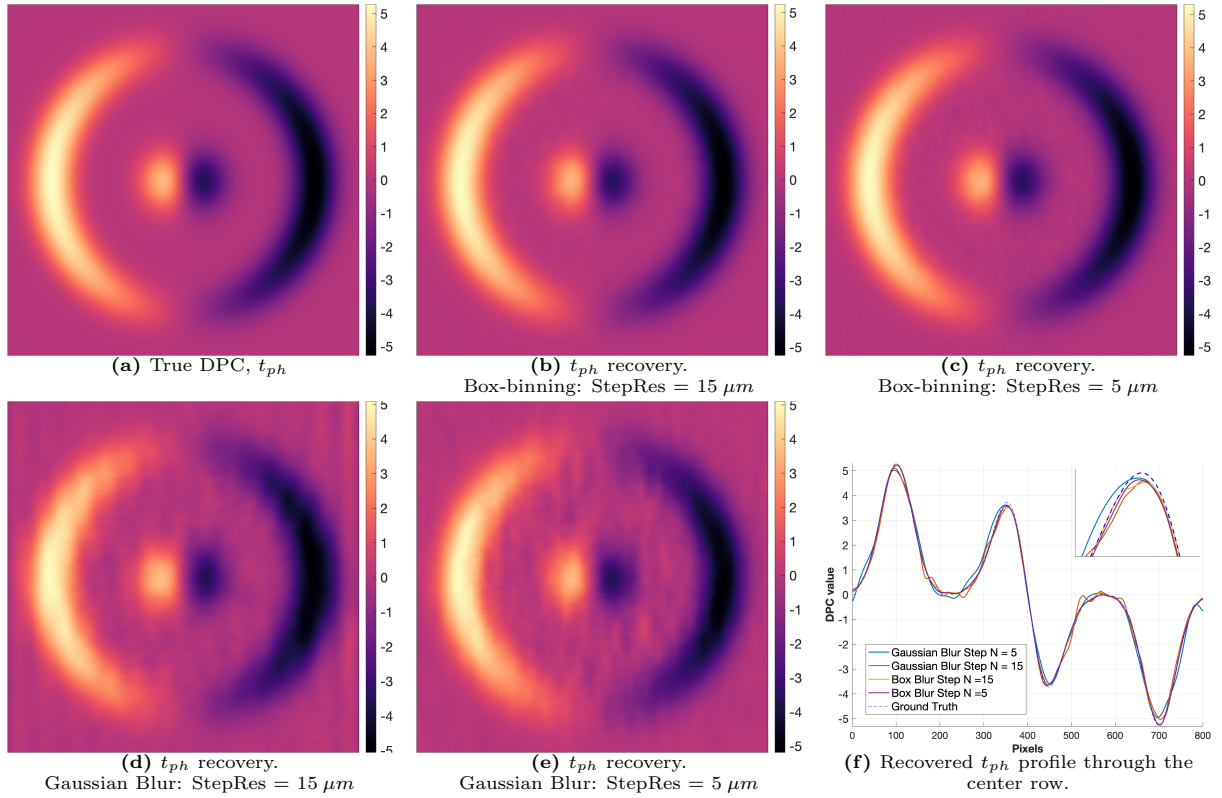


**Figure 7.** Comparison of the recovery of differential-phase for four different cases compared with the Ground Truth (GT) shown in (7a). The images are 10mm x 10mm. Line profiles of the center row are overlapped over each other in (7f) and show the minute differences in the recovery of differential phase. The difference in the lesion peak are highlighted in the inset included in (7f)

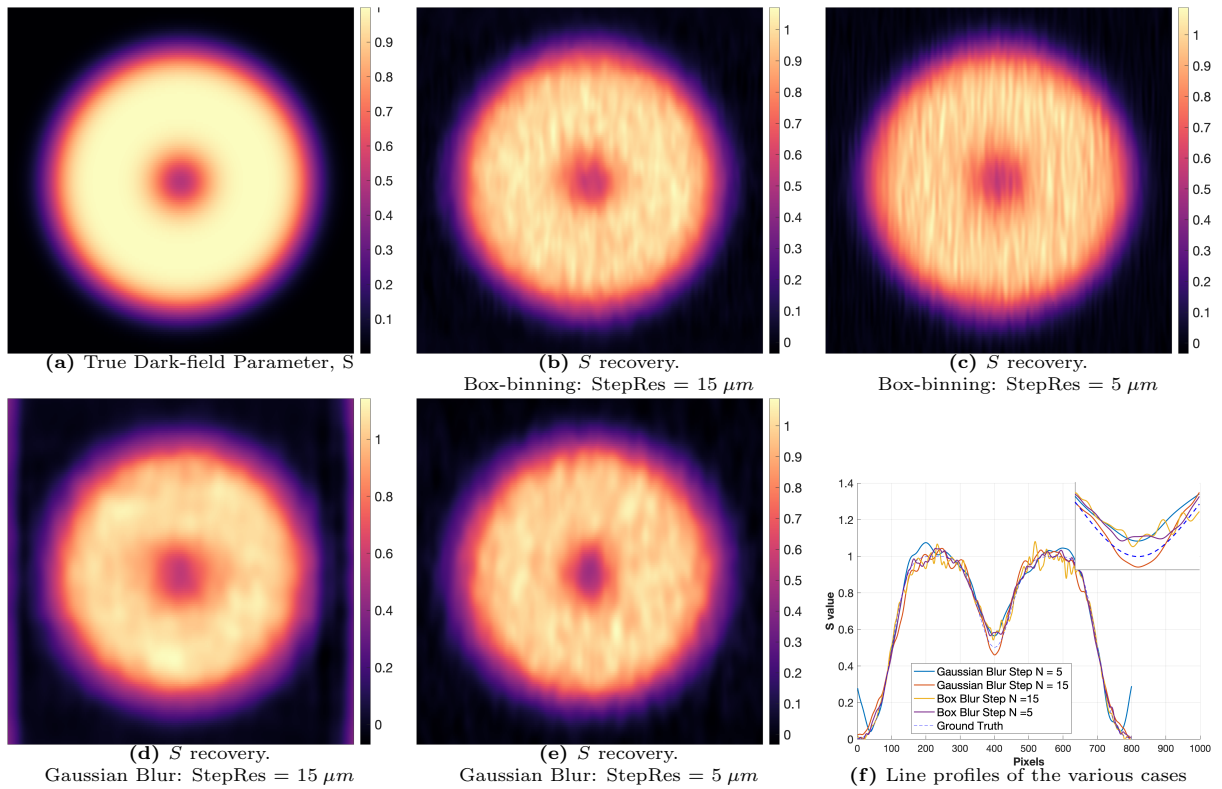


**Figure 8.** Four different cases of recovering the  $S$ .

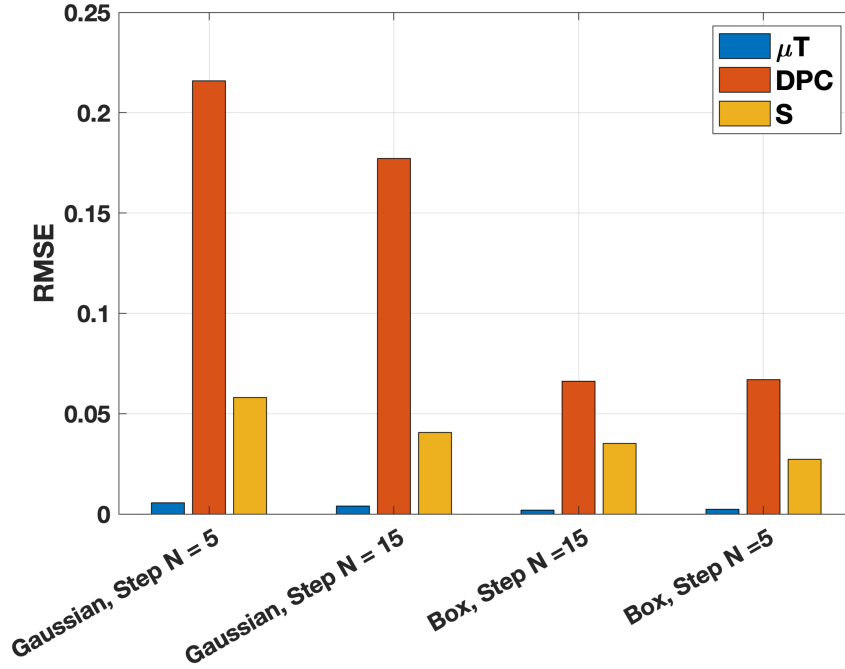


**Figure 9.** Root mean square error (RMSE) values for the four reconstruction cases, comparing  $\mu T$ , DPC, and  $S$ . Grouped bars indicate RMSE for each variable across the four cases.

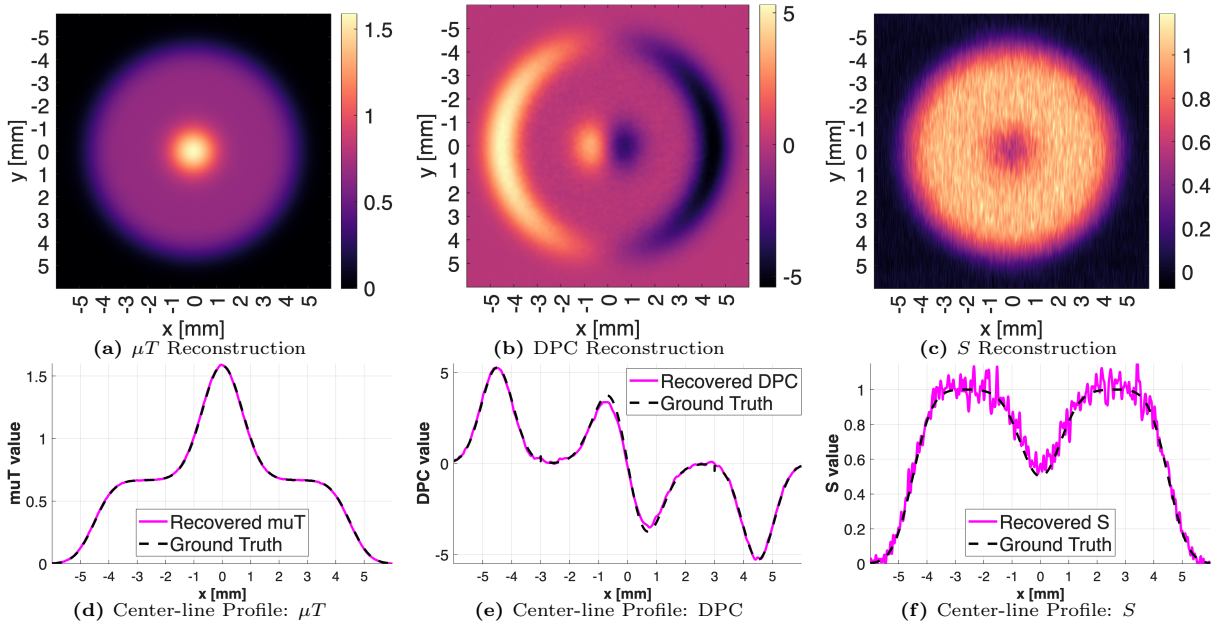


**Figure 10.** Reconstruction results for  $\mu T$ , DPC, and dark-field parameter  $S$  (top row), with corresponding center-line profiles (bottom row), for  $P_d = 13 \mu m$  and direct detector pixel size =  $30 \mu m$  with a stepping resolution =  $2 \mu m$ .

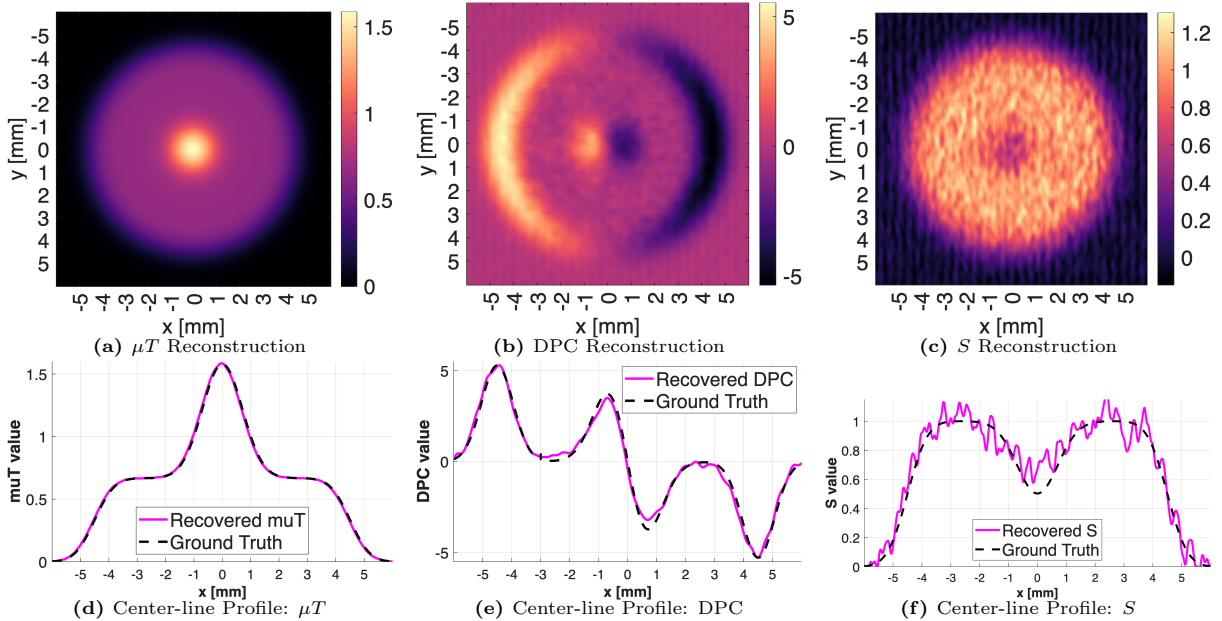


**Figure 11.** Reconstruction results for  $\mu T$ , DPC, and dark-field parameter  $S$  (top row), with corresponding center-line profiles (bottom row), for  $P_d = 22 \mu\text{m}$  with  $\pm 1 \mu\text{m}$  stepping error and direct detector pixel size =  $75 \mu\text{m}$  with a stepping resolution =  $5 \mu\text{m}$ .

## 4. Discussion

We demonstrated in simulations that super-resolution iterative reconstruction can recover radiographic attenuation, differential-phase, and dark-field images using data with different detector resolution, detector types, number of steps for analyzer-less grating systems. The quantitative comparison showed promising results: all three modalities are recoverable without the analyzer grating used in conventional Talbot-Lau X-ray interferometry.

The simulation results are shown for both direct detectors (modeled with a box-binning) and scintillator-based detectors (modeled with a Gaussian PSF). For scintillator detectors, the minimum fringe period required for reliable performance is larger, necessitating adjustments in geometry to achieve sufficient autocorrelation lengths. In the Talbot-Lau geometry, such adjustments are inherently limited by the fixed Talbot distances. In contrast, the Modulated Phase Grating Interferometer provides greater flexibility in geometry design, which may offer a distinct advantage in these scenarios.

The pixel charge-sharing was not modeled for the direct detectors, since there are automated collection techniques in detectors which aim to eliminate charge-sharing. If present, it may lead to a slight loss of fringe visibility.

Ideally, a full model of the object involves propagating through ray-tracing and including Compton Scatter, however, due to high computation cost this is not performed and an ideal projection is assumed.

Bloomer et al. [35] report a translation step of  $3 \mu\text{m}$  with a positioning accuracy of  $\pm 1 \mu\text{m}$ , demonstrating that micron-level stepping is achievable in practice. In addition, commercially available motorized translation stages (e.g., Ruf et al [36] specify  $1 \mu\text{m}$  full-step resolution (and finer effective resolution via micro-stepping), supporting the feasibility of the step sizes considered here.

However, phase stepping errors are inevitable. To estimate the phase stepping errors, we extended our simulations to include stepping uncertainty by introducing a 20% error ( $\pm 1 \mu\text{m}$ ) for a nominal  $5 \mu\text{m}$  step size, in Figure 11. Under these conditions, we were still able to successfully recover the imaging parameters, although the reconstructions exhibited some small Moiré artifacts as expected.

Our group investigated strategies for mitigating Moiré artifacts in experimental cases for MPGI as well as TLI due to phase stepping errors (Hunter et al. [37, 38]), which we reference here as a pathway for artifact suppression. Other improvements to the super-resolution reconstruction algorithm for real-world applications involve applying multi-harmonic corrections (particularly for MPGI), as demonstrated in our experimental studies [37, 38]. Such corrections, together with appropriate regularization terms, can be integrated into the iterative reconstruction framework presented here, for both the reference and

object images.

In this work, the detector is translated for phase stepping in Eqn. 2. Translating the detector is optimal for achieving sub-pixel resolution of the object because it introduces relative motion between the detector and the object. Alternatively, the grating could be translated for phase stepping and subsequent parameter recovery. In that case, the fringes move with respect to the detector as required for the super-resolution framework, but there is no relative motion between the object and the detector. Consequently, when stepping the grating instead of the detector, the recovered object parameters remain limited to the original detector resolution and do not achieve sub-pixel resolution.

One limitation of this method is that for lung imaging, or other applications requiring smaller Pd direct-conversion detectors with pixel sizes in the range of 30–75  $\mu m$  are required.

The reconstruction method implemented here can be potentially used to improve image quality in cases where the detector pixel is sufficiently small to meet the Nyquist criterion and super-resolution is not required. In this situation, phase stepping of the detector and the interlacing can still be applied to enhance resolution. The iterative reconstruction alone can recover the attenuation, differential-phase, and dark-field images and potentially outperform traditional recovery methods due to the explicit incorporation of system degradation (and potentially a noise model).

While the best performing methods for each modality were shown the same optimizers and metrics for all modalities also yield similar results, but typically with less accuracy and longer time, as shown in the Appendix.

This work considered signals from a two-dimensional simple lung phantom with realistic parameters. Future work includes extending the analysis to anatomically realistic phantoms, three-dimensional interferometric computed tomography, and ultimately experimental verification and clinical adoption.

## 5. Conclusion

Our simulations demonstrate that super-resolution can resolve attenuation, differential-phase, and dark-field images with grating interferometers even when detector sampling falls below the Nyquist rate required by traditional image recovery algorithms. Iterative reconstruction was shown to recover images of a two-dimensional lung phantom with a diseased region from simulated data. In the Talbot–Lau Interferometer, this may allow removal of the analyzer grating, thereby reducing X-ray dose. In the Modulated Phase Grating Interferometer, it permits the use of gratings with lower envelope periods, increasing the autocorrelation length, and, consequently, the sensitivity to small-angle-scatter. These methods extend applicability to cases where traditional algorithms fail, and the techniques presented here may help advance analyzer-less interferometry methods toward clinical translation.

## 6. Acknowledgments

This work is funded in part by NIH NIBIB Trail-blazer Award 1-R21-EB029026-01A1. An earlier version of this work was presented at the 67th Annual Meeting & Exhibition of the American Association of Physicists in Medicine (AAPM 2025) [39].

## 7. Author Contributions

MST constructed the two-dimensional phantom, refined the interferometric data generation and reconstruction algorithms, implemented the 2D iterative reconstructions, and performed the data analysis. HCM incorporated the differential phase parameter and contributed to the development of the initial framework and phantom. JD conceived the method, developed the initial framework, guided the algorithm development, and supervised the research. All authors contributed to the writing, discussion, and revision of the manuscript.

## 8. Conflict of Interest

JD is an inventor of two patents related to the Modulated Phase Grating Interferometry [20, 21]. JD, HCM and MST are inventors in a provisional patent related to the work in this manuscript, filed through Louisiana State University. All of the authors confirm that their work adheres to the ethical guidelines and standards for transparency and objectivity in conducting and reporting research.

## A. Appendix: Results for different optimizers

**Table 3.** Comparison of optimizers with different loss functions. The RMSE and average time to recover are shown for Gaussian modeled detector =  $75 \mu m$  and Step resolution =  $15 \mu m$  case.

	Quasi-Newton with ML		Quasi-Newton with Huber Loss	
	RMSE	Time(s)	RMSE	Time(s)
$\mu T$	0.0047	18.7	0.0068	44.7
DPC	0.22	16.1	0.91	81
$S$	0.17	2.8	0.0508	6.1

Different optimization algorithms were evaluated for parameter recovery, with the corresponding RMSE values and computation times summarized in Table 3. These results can also be compared with the RMSE values presented in Figure 9. On average, recovery of  $\mu T$  using Newton’s method with second derivatives required approximately 1 second, recovery of DPC using gradient descent with Huber loss took about 30 seconds, and recovery of  $S$  using a quasi-Newton method with Huber loss required 6.1 seconds. Although a single algorithm could, in principle, be applied to all parameters, the results demonstrate that optimal accuracy and efficiency are achieved by employing different optimizers for different parameters. The reported computation times reflect execution on a standard workstation laptop.

## References

- [1] Florian T. Gassert, Theresa Urban, Manuela Frank, et al. “X-ray Dark-Field Chest Imaging: Qualitative and Quantitative Results in Healthy Humans”. In: *Radiology* 301.2 (2021). PMID: 34427464, pp. 389–395. DOI: [10.1148/radiol.2021210963](https://doi.org/10.1148/radiol.2021210963). eprint: <https://doi.org/10.1148/radiol.2021210963>. URL: <https://doi.org/10.1148/radiol.2021210963>.
- [2] M. Bech, A. Tapfer, A. Velroyen, et al. “In-vivo dark-field and phase-contrast x-ray imaging”. In: *Scientific Reports* 3.1 (Nov. 2013), p. 3209. ISSN: 2045-2322. DOI: [10.1038/srep03209](https://doi.org/10.1038/srep03209). URL: <https://doi.org/10.1038/srep03209>.
- [3] Andre Yaroshenko, Tina Pritzke, Markus Koschlig, et al. “Visualization of neonatal lung injury associated with mechanical ventilation using x-ray dark-field radiography”. en. In: *Sci Rep* 6 (Apr. 2016), p. 24269.
- [4] A Velroyen, A Yaroshenko, D Hahn, et al. “Grating-based X-ray Dark-field Computed Tomography of Living Mice”. en. In: *EBioMedicine* 2.10 (Aug. 2015), pp. 1500–1506.
- [5] Zhentian Wang, Nik Hauser, Gad Singer, et al. “Non-invasive classification of microcalcifications with phase-contrast X-ray mammography”. In: *Nature Communications* 5.1 (May 2014), p. 3797. ISSN: 2041-1723. DOI: [10.1038/ncomms4797](https://doi.org/10.1038/ncomms4797). URL: <https://doi.org/10.1038/ncomms4797>.
- [6] Arne Tapfer, Martin Bech, Astrid Velroyen, et al. “Experimental results from a preclinical X-ray phase-contrast CT scanner”. en. In: *Proc Natl Acad Sci U S A* 109.39 (Sept. 2012), pp. 15691–15696.
- [7] Kai Scherer, Lorenz Birnbacher, Michael Chabior, et al. “Bi-Directional X-Ray Phase-Contrast Mammography”. In: *PLOS ONE* 9.5 (May 2014), pp. 1–7. DOI: [10.1371/journal.pone.0093502](https://doi.org/10.1371/journal.pone.0093502). URL: <https://doi.org/10.1371/journal.pone.0093502>.
- [8] Thomas Koehler, Heiner Daerr, Gerhard Martens, et al. “Slit-scanning differential x-ray phase-contrast mammography: proof-of-concept experimental studies”. en. In: *Med Phys* 42.4 (Apr. 2015), pp. 1959–1965.
- [9] Dan Stutman, Thomas J Beck, John A Carrino, et al. “Talbot phase-contrast x-ray imaging for the small joints of the hand”. en. In: *Phys Med Biol* 56.17 (Aug. 2011), pp. 5697–5720.
- [10] Junji Tanaka, Masabumi Nagashima, Kazuhiro Kido, et al. “Cadaveric and in vivo human joint imaging based on differential phase contrast by X-ray Talbot-Lau interferometry”. In: *Zeitschrift für Medizinische Physik* 23.3 (2013). Schwerpunkt: Röntgenbasierte Phasenkontrast Bildgebung, pp. 222–227. ISSN: 0939-3889. DOI: <https://doi.org/10.1016/j.zemedi.2012.11.004>. URL: <https://www.sciencedirect.com/science/article/pii/S0939388912001493>.
- [11] Florian T Gassert, Theresa Urban, Alexander Kufner, et al. “Dark-field X-ray imaging for the assessment of osteoporosis in human lumbar spine specimens”. en. In: *Front Physiol* 14 (July 2023), p. 1217007.
- [12] Xiayun Zhao and David W. Rosen. “Real-time interferometric monitoring and measuring of photopolymerization based stereolithographic additive manufacturing process: sensor model and algorithm”. In: *Measurement Science and Technology* 28 (2016). URL: <https://api.semanticscholar.org/CorpusID:125660749>.
- [13] Adam J. Brooks, Hong Yao, Jumao Yuan, et al. “Early detection of fracture failure in SLM AM tension testing with Talbot-Lau neutron interferometry”. In: *Additive Manufacturing* 22 (2018), pp. 658–664. ISSN: 2214-8604. DOI: <https://doi.org/10.1016/j.addma.2018.06.012>. URL: <https://www.sciencedirect.com/science/article/pii/S221486041730324X>.
- [14] V. Revol, I. Jerjen, C. Kottler, et al. “Sub-pixel porosity revealed by x-ray scatter dark field imaging”. In: *Journal of Applied Physics* 110.4 (Aug. 2011), p. 044912. ISSN: 0021-8979. DOI: [10.1063/1.3624592](https://doi.org/10.1063/1.3624592). eprint: [https://pubs.aip.org/aip/jap/article-pdf/doi/10.1063/1.3624592/13589811/044912\\_1\\_online.pdf](https://pubs.aip.org/aip/jap/article-pdf/doi/10.1063/1.3624592/13589811/044912_1_online.pdf). URL: <https://doi.org/10.1063/1.3624592>.
- [15] Atsushi Momose, Shinya Kawamoto, Ichiro Koyama, et al. “Demonstration of x-ray Talbot interferometry”. English. In: *Japanese Journal of Applied Physics* 42.7 B (July 2003), pp. L866–L868. ISSN: 0021-4922. DOI: [10.1143/jjap.42.1866](https://doi.org/10.1143/jjap.42.1866).
- [16] Atsushi Momose. “Recent Advances in X-ray Phase Imaging”. In: *Japanese Journal of Applied Physics* 44.9R (Sept. 2005), p. 6355. DOI: [10.1143/JJAP.44.6355](https://doi.org/10.1143/JJAP.44.6355). URL: <https://dx.doi.org/10.1143/JJAP.44.6355>.

- [17] Franz Pfeiffer, Timm Weitkamp, Oliver Bunk, et al. “Phase retrieval and differential phase-contrast imaging with low-brilliance X-ray sources”. In: *Nature Physics* 2.4 (Apr. 2006), pp. 258–261. ISSN: 1745-2481. DOI: [10.1038/nphys265](https://doi.org/10.1038/nphys265). URL: <https://doi.org/10.1038/nphys265>.
- [18] F. Pfeiffer, M. Bech, O. Bunk, et al. “X-ray dark-field and phase-contrast imaging using a grating interferometer”. In: *Journal of Applied Physics* 105.10 (May 2009), p. 102006. ISSN: 0021-8979. DOI: [10.1063/1.3115639](https://pubs.aip.org/aip/jap/article-pdf/doi/10.1063/1.3115639/15038269/102006_1_online.pdf). eprint: [https://pubs.aip.org/aip/jap/article-pdf/doi/10.1063/1.3115639/15038269/102006\\_1\\_online.pdf](https://pubs.aip.org/aip/jap/article-pdf/doi/10.1063/1.3115639/15038269/102006_1_online.pdf). URL: <https://doi.org/10.1063/1.3115639>.
- [19] M. Bertilson, von Hofsten O., J.S. Maltz, et al. “Analyzer-free hard x-ray interferometry”. In: *Physics in Medicine and Biology* 69.4 (2024), p. 045011. DOI: [10.1088/1361-6560/ad1f84](https://iopscience.iop.org/article/10.1088/1361-6560/ad1f84). URL: <https://iopscience.iop.org/article/10.1088/1361-6560/ad1f84>.
- [20] J. Dey, N. Bhusal, L. Butler, et al. *Phase Contrast X-ray Interferometry*. US Patent 10,872,708, Dec 22, 2020.
- [21] J. Dey, N. Bhusal, L. Butler, et al. *Phase Contrast X-ray Interferometry*. US Patent 11,488,740 B2, Nov 1, 2022.
- [22] Jingzhu Xu, Kyungmin Ham, and Joyoni Dey. “X-ray interferometry without analyzer for breast CT application: a simulation study”. In: *Journal of Medical Imaging* 7.2 (2020), p. 023503. DOI: [10.1117/1.JMI.7.2.023503](https://doi.org/10.1117/1.JMI.7.2.023503). URL: <https://doi.org/10.1117/1.JMI.7.2.023503>.
- [23] I. Hidrovo, J. Dey, H. Meyer, et al. “Neutron interferometry using a single modulated phase grating”. In: *Review of Scientific Instruments* 94.4 (Apr. 2023), p. 045110.
- [24] Hunter Meyer, Joyoni Dey, Sydney Carr, et al. “Theoretical and experimental analysis of the modulated phase grating X-ray interferometer”. In: *Scientific Reports* 14.1 (Nov. 2024), p. 26780.
- [25] Simon Spindler, Dominik Etter, Michal Rawlik, et al. “The choice of an autocorrelation length in dark-field lung imaging”. In: *Scientific Reports* 13.1 (Feb. 2023), p. 2731.
- [26] M. Strobl. “General solution for quantitative dark-field contrast imaging with grating interferometers”. In: *Scientific Reports* 4.1 (Nov. 2014), p. 7243. ISSN: 2045-2322. DOI: [10.1038/srep07243](https://doi.org/10.1038/srep07243). URL: <https://doi.org/10.1038/srep07243>.
- [27] S. Farsiu, M.D. Robinson, M. Elad, et al. “Fast and robust multiframe super resolution”. In: *IEEE Transactions on Image Processing* 13.10 (2004), pp. 1327–1344. DOI: [10.1109/TIP.2004.834669](https://doi.org/10.1109/TIP.2004.834669).
- [28] B. Gutman, M. Mrejen, G. Shabat, et al. “Angular super-resolution retrieval in small-angle X-ray scattering”. In: *Scientific Reports* 10.16038 (2020). DOI: [10.1038/s41598-020-73030-2](https://doi.org/10.1038/s41598-020-73030-2). URL: <https://doi.org/10.1038/s41598-020-73030-2>.
- [29] Till Dreier, Niccolò Peruzzi, Ulf Lundström, et al. “Improved resolution in x-ray tomography by super-resolution”. In: *Appl. Opt.* 60.20 (July 2021), pp. 5783–5794. DOI: [10.1364/AO.427934](https://opg.optica.org/ao/abstract.cfm?URI=ao-60-20-5783). URL: <https://opg.optica.org/ao/abstract.cfm?URI=ao-60-20-5783>.
- [30] Timm Weitkamp, Christian David, Christian Kottler, et al. “Tomography with grating interferometers at low-brilliance sources”. In: *Developments in X-ray Tomography V*. Vol. 6318. SPIE. 2006, pp. 249–258.
- [31] S. Marathe, L. Assoufid, X. Xiao, et al. “Improved algorithm for processing grating-based phase contrast interferometry image sets”. In: *Rev Sci Instrum* 85.1 (Jan. 2014), p. 013704.
- [32] C. G. Broyden. “The convergence of a class of double-rank minimization algorithms”. In: *Journal of the Institute of Mathematics and Its Applications* 6 (1970), pp. 76–90.
- [33] Martin Berger, J Hubbell, Stephen Seltzer, et al. *XCOM: Photon Cross Section Database (version 1.2)*. en. Jan. 1999.
- [34] M J Kitchen, D Paganin, R A Lewis, et al. “On the origin of speckle in x-ray phase contrast images of lung tissue”. en. In: *Phys Med Biol* 49.18 (Sept. 2004), pp. 4335–4348.
- [35] C Bloomer, ME Newton, G Rehm, et al. “A single-crystal diamond X-ray pixel detector with embedded graphitic electrodes”. In: *Synchrotron Radiation* 27.3 (2020), pp. 599–607.
- [36] Matthias Ruf and Holger Steeb. “An open, modular, and flexible micro X-ray computed tomography system for research”. In: *Review of Scientific Instruments* 91.11 (2020).

- [37] Hunter C. Meyer, Joyoni Dey, Conner B. Dooley, et al. “Using Higher Harmonics to Remove Grating Artifacts in Interferometry”. In: *67th Annual Meeting & Exhibition of the American Association of Physicists in Medicine (AAPM 2025)*. Poster presentation, Diagnostic and Interventional Radiology Physics Track, July 27, 2025. Washington, DC, United States, July 2025. URL: <https://aapm.confex.com/aapm/2025am/meetingapp.cgi/Paper/19460>.
- [38] Hunter C. Meyer, Joyoni Dey, Conner B. Dooley, et al. “Moiré Artifact Reduction in Grating Interferometry Using Multiple Harmonics and Total Variation Regularization”. In: *arXiv preprint arXiv:2509.16503* (2025). arXiv: [2509.16503](https://arxiv.org/abs/2509.16503) [physics.optics]. URL: <https://arxiv.org/abs/2509.16503>.
- [39] Murtuza Taqi, Joyoni Dey, and Hunter Meyer. “Analyzer-Less X-Ray Interferometry with Super-Resolution Methods”. In: *67th Annual Meeting & Exhibition of the American Association of Physicists in Medicine (AAPM 2025)*. Poster presentation, Diagnostic and Interventional Radiology Physics Track, July 27, 2025. Washington, DC, United States, July 2025. URL: <https://aapm.confex.com/aapm/2025am/meetingapp.cgi/Paper/17378>.